JASA ARTICLE

Three-dimensional echo decorrelation monitoring of radiofrequency ablation in *ex vivo* bovine liver

E. Ghahramani Z, P. D. Grimm, K. J. Eary, M. P. Swearengen, E. G. Sunethra K. Dayavansha, and T. D. Mast[a)]
Department of Biomedical Engineering, University of Cincinnati, Ohio 45267-0586, USA

ABSTRACT:
Three-dimensional (3D) echo decorrelation imaging was investigated for monitoring radiofrequency ablation (RFA) in *ex vivo* bovine liver. RFA experiments ($N = 14$) were imaged by 3D ultrasound using a matrix array, with in-phase and quadrature complex echo volumes acquired about every 11 s. Tissue specimens were then frozen at −80 °C, sectioned, and semi-automatically segmented. Receiver operating characteristic (ROC) curves were constructed for assessing ablation prediction performance of 3D echo decorrelation with three potential normalization approaches, as well as 3D integrated backscatter (IBS). ROC analysis indicated that 3D echo decorrelation imaging is potentially a good predictor of local RFA, with the best prediction performance observed for globally normalized decorrelation. Tissue temperatures, recorded by four thermocouples integrated into the RFA probe, showed good correspondence with spatially averaged decorrelation and statistically significant but weak correlation with measured echo decorrelation at the same spatial locations. In tests predicting ablation zones using a weighted K-means clustering approach, echo decorrelation performed better than IBS, with smaller root mean square volume errors and higher Dice coefficients relative to measured ablation zones. These results suggest that 3D echo decorrelation and IBS imaging are capable of real-time monitoring of thermal ablation, with potential application to clinical treatment of liver tumors. © *2022 Acoustical Society of America*. https://doi.org/10.1121/10.0011641

(Received 7 January 2022; revised 14 May 2022; accepted 23 May 2022; published online 9 June 2022)

[Editor: Bradley E. Treeby] Pages: 3907–3918

I. INTRODUCTION

Radiofrequency ablation (RFA), a method in which alternating electric current causes ion agitation in tissue resulting in heating and coagulative necrosis, is a common treatment for nonresectable liver tumors, including hepatocellular carcinoma (HCC) and colorectal metastases,[1–3] and has been considered the most widely used method of image-guided local thermal ablation for HCC up to 5 cm diameter.[4] Although RFA can provide survival rates comparable to surgical resection, frequency of local tumor recurrence after RFA can be higher than surgery.[5,6] Real-time monitoring of ablation progress may help to avoid incomplete RFA treatments and resulting local recurrence of tumors and is an active area of research.[3,7]

Magnetic resonance imaging has been used for monitoring thermal ablation by real-time magnetic resonance thermometry, although this approach can be costly and inconvenient.[8] Another ablation monitoring method is computed tomography-guided RFA, which provides better edge detection of ablated lesions,[9] but also has downsides such as long procedure time, radiation exposure, potential contrast-induced nephropathy, and higher cost.[10]

Ultrasound guidance of RFA has advantages of lower cost, portability, and real-time operation. Pulse-echo ultrasound guidance methods for RFA and other thermal ablation approaches have included conventional B-mode (brightness mode) imaging,[11] contrast-enhanced B-mode imaging,[12] echo energy-based methods such as integrated backscatter imaging,[13] and cross correlation-based methods such as elastography,[14,15] thermal strain imaging,[16–19] and thermal expansion imaging.[20] The latter methods quantify strain within pulse-echo scan lines, caused by applied mechanical stress,[14,15] temperature dependence of sound speed,[16–19] and local expansion of tissue from heating and coagulation.[20] However, while thermal ablation is under way, many potential pulse-echo ultrasound monitoring methods are limited by inconsistent, transient heat-induced changes in tissue reflectivity,[21] pulse-echo signal decorrelation[22] due to vapor bubble activity and tissue state changes,[21] and complex dependence of tissue acoustic and viscoelastic properties on temperature.[17,23,24]

Echo decorrelation imaging, a computationally efficient method that spatially maps heat-induced changes in ultrasound echoes over millisecond time scales,[21,25] can potentially provide feedback on ablation progress while RFA energy is being delivered. In this method, echo changes are first quantified by the local decorrelation of beamformed pulse-echo scan lines, then tracked over the duration of thermal ablation to generate cumulative echo decorrelation maps. Implementations of echo decorrelation imaging using two-dimensional (2D) ultrasound data have proven successful for monitoring RFA of *ex vivo*[21] and *in vivo*[25] tissue as

[a)]Electronic mail: doug.mast@uc.edu

well as microwave ablation,[26] bulk ultrasound ablation,[27] and high-intensity focused ultrasound (HIFU).[28–31]

Because RFA and similar bulk thermal ablation methods treat large volumes of heterogeneous tumor tissue simultaneously, 2D imaging is insufficient to monitor ablation progress during RFA treatments. This issue may be even more significant when treating multiple neighboring tumors simultaneously. To fully characterize ablation throughout the targeted ablation volume, real-time three-dimensional (3D) monitoring during the ablation process would be useful to confirm treatment success, while avoiding overtreatment causing complications.[7,32]

Here, 3D echo decorrelation imaging is implemented and tested on RFA of *ex vivo* bovine liver tissue. These tests employed 3D ultrasound imaging using a clinical ultrasound scanner that achieves volumetric frame rates comparable to 2D ultrasound. However, compared to 2D echo decorrelation imaging, this 3D configuration requires sparser spatial sampling of the image volume, as well as acquisition of much larger echo data sets, thus limiting both spatial and temporal resolution. The research reported here aimed to test whether, given these limitations, 3D echo decorrelation imaging can successfully predict local tissue ablation from echo data acquired while ablation is progress. Receiver operating characteristic (ROC) curve analysis was used to quantify the success of local ablation prediction. Secondary analyses correlated local echo decorrelation with corresponding local tissue temperatures and tested the feasibility of predicting ablation volumes using weighted K-means clustering on 3D echo decorrelation and integrated backscatter (IBS) maps. Toward optimization of real-time thermal ablation monitoring, these analyses were performed and compared for three alternative definitions of echo decorrelation employing different normalization approaches, as well as for IBS.

II. MATERIALS AND METHODS

A. Ablation Experiments

As fixtures for RFA experiments with 3D ultrasound imaging, a cuvette (100 mm height, 82 mm width, 82 mm depth) and matching stand were designed and 3D-printed with polylactic acid (PLA) filament [Fig. 1(a)]. A window for placement of an ultrasound array [Fig. 1(b), G] was sealed with a Tegaderm film adhesive membrane (3M Health Care, St. Paul, MN). The top of the cuvette was partially closed with a lid integrating a 6 cm guide [Fig. 1(b), C], through which the RFA needle (RITA StarBurst XLi-enhanced device with micro-infusion, AngioDynamics, Latham, NY) was inserted straight into the tissue. A lock attached to the RFA needle [Fig. 1(b), B] insured insertion to a depth of 60 mm from the lid's inner surface. As shown in Fig. 1(b), the resulting location of the RFA probe tip was 52 mm from the window and imaging probe surface (z or range direction), centered on the ultrasound array's axis at 42 mm from the cuvette sides (y or azimuth direction), and 40 mm from the inner bottom surface of the cuvette (elevation direction),

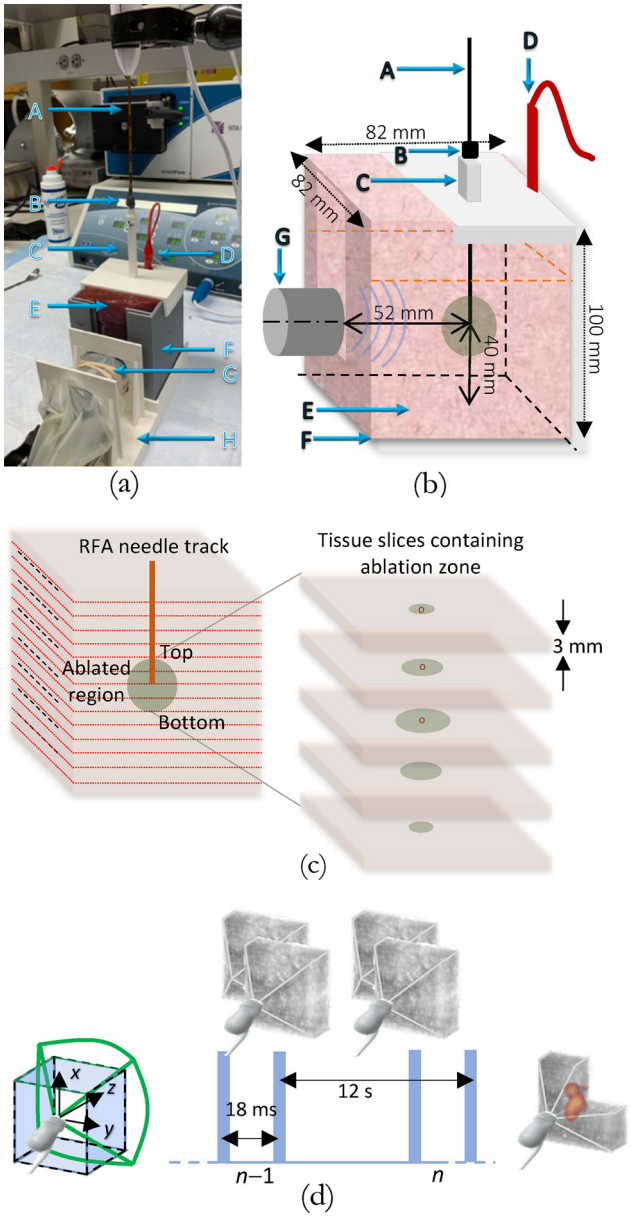

FIG. 1. (Color online) Experimental setup and data acquisition. (a) Photograph of the setup with labeled components the RFA probe (A), probe lock (B), needle guide (C), grounding wire (D), tissue specimen (E), cuvette (F), 4Z1c array (G), and 3-D printed fixture (H). (b) Illustration of the transducer, probe, and tissue geometry with the same labeled components. (c) Illustration of tissue sectioning. Left, tissue block showing parallel surface cuts for distance reference (dashed black lines), the RFA needle track (solid red line), ablated region (gray circle), and cuts between parallel sections (dotted red lines). Right, tissue sections spanning the ablated region, showing cross-sections of the ablated region (gray circles) and the RFA needle track (red circles). (d) Configuration for acquisition and processing of image data, showing a sketch of the frustum-shaped echo volume (green), the cuvette boundaries (blue), the coordinate system with origin centered on the array surface (z, range; y, azimuth; x, elevation), and timing of echo volume acquisition and processing.

with positioning uncertainty of about 1 mm. Behind the guide, a small slit in the box lid enabled the connection of the RFA generator's electrical ground to a grounding pad, cut from clinical dispersive electrodes (RITA® Thermopads, AngioDynamics, Manchester, GA) specified for use with

the same generator and ablation probe. The stand integrated mounts for the ultrasound transducer and the cuvette, designed to keep both secured in the intended geometry while also enabling rapid switching between ablation experiments.

Fresh whole bovine liver was obtained from a local slaughterhouse and kept in ice inside a cooler while transporting to the laboratory for ablation experiments. The liver was stored in a sealed bag on the benchtop for less than 30 min to acclimate to room temperature (between 20 °C and 25 °C). Liver tissue was then cut into roughly cubic specimens fitting the width and length of the cuvette with height 70–90 mm and placed into the cuvette, with a grounding pad bounding the tissue edge distal to the ultrasound array. After securing the stand in place using a 3D positioning arm, the cuvette containing bovine liver was placed and locked onto it. To minimize air bubbles within the tissue, phosphate-buffered saline (0.01 M, pH 7.4 at 25 °C, Sigma Life Science P3813, St. Louis, MO) was poured into the cuvette while the tissue was manually manipulated, allowing saline to penetrate empty blood vessels. The RFA probe was inserted through the lid's integrated needle guide into the tissue and secured with another 3D positioning arm [Fig. 1(a)]. The RFA probe was deployed to 2 cm diameter and a grounding wire was connected to the grounding pad through the opening on the lid.

For ablation exposures ($N = 14$), the RFA generator (RITA® 1500X RF Generator, AngioDynamics, Manchester, GA) was set to nominal power 150 W and target temperature 105 °C. Duration for maintaining this target temperature, averaged between three thermocouples located within tips of the RFA probe tines, was set to 5 min in the RFA generator. The resulting duration of each ablation procedure was about 10 min, including approximately 2 min of initial heating, 5 min of tissue being held at the target temperature, and 2 min of cooldown.

Throughout each procedure, time-dependent temperatures recorded automatically by the RFA generator from four thermocouples integrated into the RFA probe (three thermocouples within tine tips, as well as a fourth thermocouple extending from the needle tip), were acquired from the generator's RS232 port output (baud rate 9600) at a sampling rate of 10 Hz using a custom program written in C++ and run on a laptop computer. Data packets, which also included output of elapsed time, instantaneous electrical power, measured tissue impedance, and generator mode parameters, were acquired by the receiving computer, filling a buffer after detection of a specific character sequence ending with a "C" (end of text) character within the serial data stream. Temperature values, output as 14-bit integers stored within two-byte words after scaling by a factor of 10, were parsed to record time-dependent temperature measurements from each thermocouple with 0.1 °C precision.

After each ablation procedure, a fitted sliding cover was inserted into the cuvette's window and a tightly fitting lid was placed on the top opening, both of which constrained expansion of the liver tissue during freezing. The cuvette was then placed in a −80 °C freezer for at least 12 h. After removal from the freezer, the window cover and lid were removed. For use as a height reference, multiple parallel cuts were made on the tissue surface within the window at intervals of 5 mm, using a scalpel and ruler.

Frozen tissue specimens were sectioned into parallel slices, starting from the bottom of the tissue block (lower elevation), using a commercial meat slicer [Fig. (c)]. The parallel cuts on the vertical tissue block surface (spacing 5 mm) were used as distance references for the observable top and bottom of the ablation zone, assessed based on gross discoloration. The average slice thickness for each experiment (typically 3 mm) was found from the number of tissue sections covering this measured span. The elevational position of the RFA needle tip was determined from the bottommost tissue section in which the needle track could be observed; this elevation position within the tissue volume was registered to the known elevation position of the needle tip, level with the ultrasound array axis and 40 mm from the inner bottom surface of the cuvette. Since water content within the ablation zone was small compared to the surrounding liver parenchyma, expansion of the ablation zone due to freezing was neglected.

After sectioning, tissue was optically scanned at a resolution of 240 dpi (V550, Epson America, Inc. Long Beach, CA). Scanned tissue sections were then segmented using a custom tissue segmentation graphical user interface (GUI). Within this GUI, the scanned image of each tissue section was manually translated and rotated to best match a fixed square outline corresponding to the cuvette's cross section. Ablation zones were primarily segmented automatically using an empirically defined brightness threshold determining ablated region. In a few trials, manual segmentation was performed due to ambiguities in image brightness caused by large vessels near the ablation zone boundaries. A 3D map of the ablation zone was then reconstructed using nearest-neighbor interpolation onto a grid with an isotropic step size of 1 mm for direct comparison to 3D echo decorrelation and IBS maps.

B. Ultrasound data acquisition

For 3D pulse-echo imaging of tissue during RFA, a clinical matrix ultrasound phased array (active aperture $19.2 \times 14.4\,\mathrm{mm}^2$; 48×36 elements; bandwidth 1.5–3.5 MHz) and imaging system (4Z1c matrix array and Acuson SC2000 scanner, Siemens, Erlangen, Germany) were used with center frequency 2.8 MHz, imaging depth 110 mm, and frame rate 55 volumes per second. Throughout each ablation experiment, pairs of sequential echo volumes (separated by the inter-frame time of 18 ms) were acquired and stored by the scanner, with one pair of volumes stored approximately every 12 s [Fig. 1(d)]. Each volume comprised a $79° \times 79°$ pyramid with 55×54 (azimuth × elevation) demodulated, complex (in-phase/quadrature or IQ) scan lines of length 376 samples and sampling rate 2.5 MHz. This acquisition size ensured that

the entire ablated region was within the pyramidal image volume in all cases.

All processing of image data were performed in MATLAB (The MathWorks, Natick, MA). Scan conversion from the scanner's pyramidal (frustum) coordinate system to a 3D Cartesian coordinate system was performed using the known positioning of scan lines. As confirmed with the manufacturer, scan lines were spaced in equal increments of $\sin(\theta)$ and $\sin(\varphi)$ in the azimuth and elevation directions, defined as angles from the xy and xz planes, respectively. Corresponding relations between the frustum coordinates (r, θ, φ) and Cartesian coordinates (x,y,z) are

$$r = \sqrt{x^2 + y^2 + z^2}, \quad \sin(\theta) = \frac{y}{\sqrt{y^2 + z^2}}, \quad \sin(\varphi) = \frac{x}{\sqrt{x^2 + z^2}}. \tag{1}$$

For scan conversion, coordinates of each sample were first determined in the pyramidal coordinate system. A Cartesian grid with isotropic step size of 1 mm was then defined and the pyramidal coordinates of each grid point were determined. The sampled volumes of complex echo data were then scan-converted onto the Cartesian grid using trilinear interpolation within the pyramidal coordinate system.

C. Echo decorrelation computation

For monitoring the thermal ablation process in three dimensions, echo decorrelation imaging was extended to 3D. All computations of echo decorrelation and IBS maps were performed within a spherical region of interest with diameter 4 cm (corresponding to the targeted ablation zone diameter of 2 cm plus a 1 cm radial margin), centered at the known position of the RFA needle tip. This computation starts with zero-lag, spatially windowed cross correlation between sequential complex echo volumes I_0 and I_1,

$$R_{01}(\boldsymbol{r}, n) = \langle I_0(\boldsymbol{r}, n)^* I_1(\boldsymbol{r}, n)\rangle = \iiint w(\boldsymbol{r} - \boldsymbol{r}')\, I_0(\boldsymbol{r}', n)^* I_1(\boldsymbol{r}', n)\, dV', \tag{2a}$$

$$w(r) = e^{-r^2/2\sigma^2}, \tag{2b}$$

where temporal indices n sequentially number each acquired echo volume pair, $\boldsymbol{r}$ is a position vector within an echo volume, $I_0(\boldsymbol{r})^*$ is the complex conjugate of echo volume I_0, and dV' is a differential volume element corresponding to the vector integration variable $\boldsymbol{r}'$. In the following, angle brackets denote the same operation of convolution with a Gaussian window with width parameter σ. Choice of this width parameter specifies size of the 3D correlation window employed (e.g., full width at half maximum 2.355σ), so that larger σ values reduce spatial resolution of echo decorrelation images but increase averaging of spatially random variations.[33]

Corresponding zero-lag, spatially windowed autocorrelations of complex echo volumes are defined as

$$R_{00}(\boldsymbol{r}, n) = \left\langle |I_0(\boldsymbol{r}, n)|^2 \right\rangle, R_{11}(\boldsymbol{r}, n) = \left\langle |I_1(\boldsymbol{r}, n)|^2 \right\rangle, \tag{3}$$

$$\beta^2(\boldsymbol{r}, n) = R_{00}(\boldsymbol{r}, n) R_{11}(\boldsymbol{r}, n). \tag{4}$$

Locally normalized echo decorrelation[33,34] is then given as a normalized correlation coefficient subtracted from unity divided by inter-frame time τ,

$$\Delta_L(\boldsymbol{r}, n) = \frac{1}{\tau}\left(1 - \frac{|R_{01}(\boldsymbol{r}, n)|^2}{\beta^2(\boldsymbol{r}, n)}\right) = \frac{\beta^2(\boldsymbol{r}, n) - |R_{01}(\boldsymbol{r}, n)|^2}{\tau[\beta^2(\boldsymbol{r}, n)]}. \tag{5}$$

This definition of decorrelation is equivalent to some used in previous studies of focused ultrasound ablation[29,31] and in computational analysis of echo decorrelation imaging, which has related echo decorrelation to decoherence of the scattering medium reflectivity.[33,34] Normalization by the inter-frame time τ accounts for observed increases in echo decorrelation vs temporal lag, consistent with expected continuous heat-induced changes in tissue structure.

Since echo decorrelation as defined by Eq. (5) can become large due to electronic noise within hypoechoic regions, a *globally normalized echo decorrelation* can also be defined, normalized by a spatial mean of the autocorrelation product within the imaged ROI,

$$\Delta_G(\boldsymbol{r}, n) = \frac{\beta^2(\boldsymbol{r}, n) - |R_{01}(\boldsymbol{r}, n)|^2}{\tau[\overline{\beta^2}(n)]}. \tag{6}$$

Echo decorrelation as defined by Eq. (6) tends to be larger in regions with greater tissue reflectivity. As a compromise between artifacts associated with tissue echogenicity in the definitions of Eqs. (5) and (6), a *combined echo decorrelation* parameter has also been defined,[21,25–28,30,35]

$$\Delta_c(\boldsymbol{r}, n) = \Delta(\boldsymbol{r}, n) = 2\left[\frac{\beta^2(\boldsymbol{r}, n) - |R_{01}(\boldsymbol{r}, n)|^2}{\tau[\beta^2(\boldsymbol{r}, n) + \overline{\beta^2}(n)]}\right]. \tag{7}$$

By any of these definitions, echo decorrelation represents local deviations between a pair of complex (IQ) image volumes per unit inter-frame time, here $\tau = 18$ ms. The resulting echo decorrelation maps are zero in regions with no change in pulse-echo image data and maximum in regions where local echo changes were greatest. To track all measured changes in echo volumes, cumulative echo decorrelation is defined as the temporal maximum decorrelation at each position $\boldsymbol{r}$, for each of these definitions [Eqs. (5)–(7)].

For comparison, relative IBS images were defined as the decibel-scaled ratio between the square root of the image autocorrelation product, $\beta(\boldsymbol{r}, n)$ at the current and first recorded image volume pairs,[21,25]

$$\mathrm{IBS}(\boldsymbol{r}, n) = 10 \cdot \log_{10}\left(\frac{\beta(\boldsymbol{r}, n)}{\beta(\boldsymbol{r}, 1)}\right), \tag{8}$$

thus, mapping increases in local echogenicity relative to the tissue before RFA. IBS images were computed from the

same pulse-echo image data and accumulated in the same manner as echo decorrelation images.

B-Mode images were constructed from logarithmically scaled envelopes $10 \cdot \log_{10}[|I_1(\boldsymbol{r})|]$ of the IQ scan lines and displayed using a 65 dB dynamic range. For displaying decorrelation and IBS maps, duplex B-mode/echo decorrelation and B-mode/IBS images were constructed by overlaying the grayscale B-mode image with a pseudocolor image of the $\log_{10}$-scaled echo decorrelation per millisecond or the decibel-scaled integrated backscatter, respectively. Transparency of the echo decorrelation and IBS overlays were proportional to the logarithmically scaled parameters mapped over a defined dynamic range.

D. Data analysis

For direct comparison of 3D echo decorrelation and IBS images with ablated tissue histology, ROC curve analysis was utilized as previously performed for 2D echo decorrelation imaging.[21,25,27,35] Segmented maps of ablated tissue across all 14 trials were compared voxel-by-voxel with measured echo decorrelation and IBS parameters within a spherical ROI of radius 20 mm centered at the tip of the RFA needle. This choice of ROI included both the targeted ablation zone of radius 10 mm and an additional 10 mm margin, beyond which the tissue was assumed to be unablated. ROC curves plot true-positive ratio vs false-positive ratio for prediction of local ablation, as a parametric function of the parameter threshold. Area under the ROC curve (AUC) is 1 for perfect prediction of all ablated voxels and 0.5 for prediction equivalent to chance. Optimal thresholds for ablation prediction for all predictors were defined as those corresponding to the point nearest the top left-hand corner of the ROC plot,[36] simultaneously maximizing the sensitivity and specificity of the predictor.

To optimize ablation prediction with respect to tradeoffs between spatial resolution and stochastic averaging,[33,34] AUC for combined echo decorrelation [Eq. (7)] was computed as a function of the correlation window width parameter σ over the range 1–8 mm. The maximum AUC was obtained for $\sigma = 3$ mm, and this value of σ was used in all subsequent analysis. Notably, AUC for combined echo decorrelation was insensitive to choice of this parameter, such that the difference between minimum and maximum AUC was about 0.04 over the investigated range.

Using MATLAB, AUC values were compared to the null hypothesis (AUC = 0.5) and the statistical significance was calculated by a one-tailed Z test employing a general model for the AUC standard error (one-tailed, significance criterion $p < 0.05$).[37] Statistical significance of differences between AUC values for all normalizations of echo decorrelation and IBS was calculated using R (pROC package, R Foundation for Statistical Computing, Vienna, Austria) and the method of DeLong *et al.*[38] (two-tailed paired tests, significance criterion $p < 0.05$). For assessments of statistical significance, an effective number of independent ablation predictions N_{eff} was determined from the total number of predicted voxels N_{total} and the maximum hexagonal packing density of spheres with diameter $d = 2.355\ \sigma$,[25] resulting in $N_{\text{eff}} = \sqrt{2}(l/d)^3 N_{\text{total}}$, where $l = 1$ mm is the isotropic step size of the Cartesian grid employed. To account for this estimated number of independent predictions, Z statistics were scaled by the factor $(N_{\text{eff}}/N_{\text{total}})^{1/2}$ and effective p values (significance criterion $p < 0.05$, two-tailed) were then determined using the cumulative distribution function of the standard normal distribution.

To assess the dependence of echo decorrelation and IBS parameters on local tissue temperature, measurements from four thermocouples integrated into the RFA probe were correlated with echo decorrelation and IBS values at the known thermocouple locations. This temperature dependence was visualized using histogram plots of predictor values vs co-located measured temperature and quantified by linear regression between logarithmically scaled predictors and local temperature. Statistical significance of predictor-temperature relationships was assessed based on the cumulative distribution function of the Pearson correlation coefficient r.

The potential utility of these imaging methods for predicting ablation zone margins and volumes was assessed using weighted K-means clustering.[39] This approach was designed to provide an unsupervised segmentation of ablation zones based on objective data, while incorporating *a priori* knowledge that tissue nearer the RFA probe tip is more likely to be ablated. Voxels within the computational ROI of 20 mm radius, centered at the tip of the RFA probe, were characterized by two features for each image-based predictor: (1) the logarithmically scaled predictor ($\log_{10}$-scaled decorrelation/ms or IBS) and (2) Euclidean distance r from the RFA probe tip, across all trials. Each feature was scaled using linear min-max normalization, such that scaled values ranged between 0 and 1. Clustering in this 2D feature space was then performed for $K = 2$ clusters, with the inner cluster (smaller distance from the probe tip) classified as ablated and the outer cluster classified as unablated.

To initiate the K-means iteration, centroids for the two clusters were initialized as points within the feature space considered most and least likely to be ablated, respectively. The initial centroid for the ablated cluster was placed with feature (1) at the maximum predictor value within a small spherical region around the RFA probe tip ($r \leq 0.2$ mm) and feature (2) at the normalized Euclidean distance 0. The initial centroid for the unablated cluster was chosen with feature (1) at the minimum predictor value within the spherical shell $19.8 \leq r \leq 20$ mm and feature (2) at the normalized Euclidean distance 1.

To iteratively update the two clusters, Euclidean distances from the two centroids were computed for all points within the 2D feature space and data points were assigned to their nearer centroid. The two centroids were then updated within each respective cluster to place feature (1) at its mean value and feature (2) at its mean value multiplied by a weight w. This weight was intended to account for the skewness of feature (2), i.e., the much higher prevalence of voxels at higher distances from the probe tip. These iterations were repeated until the average volume prediction error

across all trials was less than 10%, up to a maximum of 15 iterations.

Predicted ablation zone volumes, defined as the summed volume of all voxels within the ablated cluster, were compared to measured ablation zone volumes for each experiment ($N = 14$). To find an appropriate weight for minimization of volume prediction error, the clustering process was repeated for a vector of weights $0.4 \leq w \leq 1$ with step size 0.05 and the root mean square (RMS) error of volume prediction was assessed across all 14 trials. For the final choice of weight w, RMS error in ml, normalized RMS error (expressed as a percentage of RMS measured volume), and correlation coefficients of predicted vs measured volumes were computed.

To assess agreement of predicted and measured ablation zone margins, Dice coefficients[40] were computed between the ablation zones segmented manually from scanned tissue sections and those predicted by weighted K-means clustering of predictor values and distances from the RFA probe tip. Dice coefficients were compared between predictors using two-tailed, paired Student t tests with the significance criterion $p \leq 0.05$.

III. RESULTS

3D echo decorrelation and IBS images are shown in Fig. 2 with corresponding ablated tissue histology for two representative trials. The first row of each panel shows parametric images of combined echo decorrelation, locally and globally normalized echo decorrelation, and IBS superimposed on corresponding cross-sections of the B-mode image volume as well as an optically scanned and segmented section of the ablated tissue volume, all at the elevation position nearest the RFA needle tip. Inner boundaries of the cuvette are visible in the B-mode images as bright borders around the echo volume. The second row of each panel shows isosurface renderings of the same parameters and the ablated tissue volume with corresponding perpendicular cross-sections of the pyramidal B-mode image volume. Decorrelation isosurfaces are plotted at the value $10^{-3.0}$/ms, while IBS isosurfaces are plotted at the value 4.0 dB.

The parametric images, as well as their isosurface renderings shown in Fig. 2, generally correspond well with ablation zones seen in the corresponding tissue sections and isosurface renderings of the segmented 3D ablation zone. The best correspondence is seen for globally normalized echo decorrelation [Eq. (6)], which generally shows high values in voxels in which ablation occurred. Locally normalized and combined echo decorrelation maps [Eqs. (5) and (7), respectively] were also consistent with the corresponding ablated tissue histology. However, IBS maps [Eq. (8)] were less consistent, showing some low values within observed ablation zones. General correspondence can be seen between echo decorrelation maps and the ablation zone.

Results of ROC curve analysis, assessing prediction of local ablation by echo decorrelation and IBS imaging, are shown in Fig. 3 and Table I. All four image parameters predicted local ablation significantly better than chance ($p < 10^{-16}$). Globally normalized echo decorrelation showed the highest predictive capability (AUC = 0.837), while IBS showed the lowest predictive capability (AUC = 0.719). AUC for locally normalized echo decorrelation was statistically equivalent to IBS ($p = 0.704$); all other AUC values were significantly different from one another ($p < 10^{-5}$), with prediction performance of combined echo decorrelation (AUC = 0.801) falling between locally and globally normalized decorrelation. Optimal thresholds for prediction of local ablation were similar for the three definitions of echo decorrelation investigated, ranging from −3.71 to −3.57 ($\log_{10}\Delta$/ms).

Temperatures from four thermocouples integrated into the RFA probe, together with simultaneous instantaneous and cumulative combined echo decorrelation averaged within the computational ROI, are plotted vs time in Fig. 4. Thermocouples T1, T2, and T3 were located at the nominal boundary of the expected ablation zone (10 mm from the RFA needle axis for a probe deployment of 20 mm diameter), while T4 was located outside the expected ablation zone, 15 mm below the RFA needle tip in the elevation direction. Thus, T4 generally measured a lower temperature than the other three thermocouples. During about the first 2 min of RFA treatment, tissue temperature and echo decorrelation tended to increase together. After the RFA generator held tissue at the set target temperature of 105 °C (about 2–7 min of treatment), instantaneous and cumulative echo decorrelation parameters tended to stabilize. After completion of RFA treatment (about 7–9.5 min), the instantaneous echo decorrelation tended to decline.

Figure 5 shows a 2D histogram plot of instantaneous measured values for all four predictors vs time-dependent measured temperature, evaluated at the locations of the four integrated thermocouples at all time points within all 14 ablation trials. Also, shown as superimposed dashed lines are the lines of best fit for $\log_{10}$-scaled echo decorrelation and dB-scaled IBS vs temperature, computed by linear regression. All four predictors were significantly but weakly correlated with tissue temperature ($p < 10^{-15}$, $N = 3360$). The correlation coefficient between local predictors and local temperature was smallest for locally normalized echo decorrelation (0.435) and largest for globally normalized echo decorrelation (0.519).

For prediction of ablation zone volumes using the weighted K-means clustering approach, optimal weights w typically fell within the range $0.7 \leq w \leq 0.9$ for all four predictors, with results not highly sensitive to the weight value. The minimum average volume prediction error, computed across all trials and all four predictors, was near zero for $w = 0.8$ and was <0.5 ml for $0.7 \leq w \leq 0.9$. All further analysis employed the weight $w = 0.8$. For each predictor, Fig. 6 shows scatter plots of the final clusters classified as ablated and unablated with their respective centroids across all 14 trials, scatter plots of predicted vs measured ablation zone volumes across all 14 trials, and cross-sections of

https://doi.org/10.1121/10.0011641

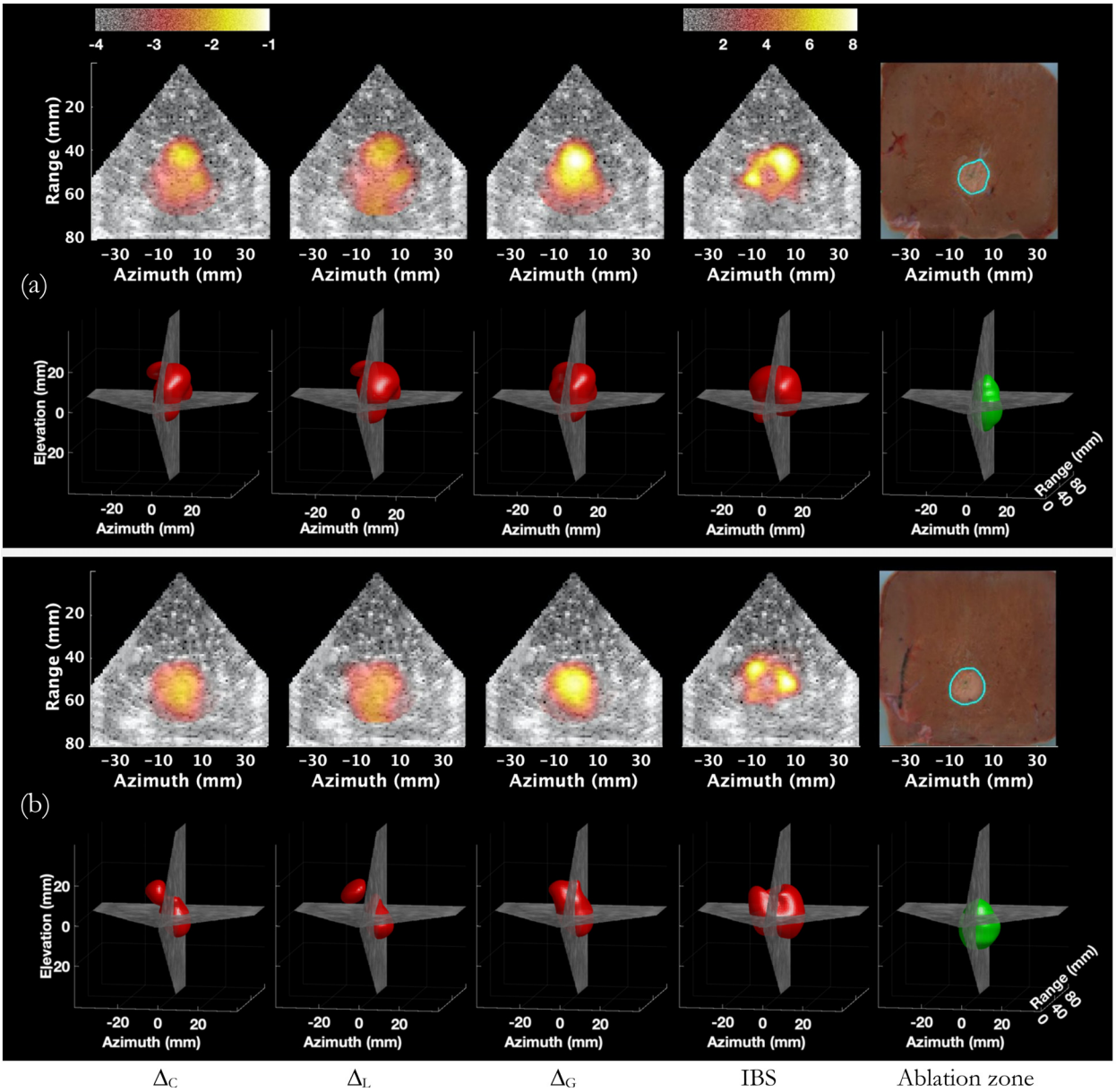

FIG. 2. (Color online) Representative 2D and 3D B-mode and echo decorrelation images with corresponding tissue histology for two representative trials, (a) and (b). The first row of each panel shows cross-sections at zero elevation, while the second row shows 3D isosurface renderings superimposed on perpendicular cross-sections of the B-mode image volume. Columns show, from left to right, combined echo decorrelation (Δ_C), locally normalized echo decorrelation (Δ_L), globally normalized echo decorrelation (Δ_G), decibel-scaled IBS, and segmented ablation zones based on optical scans of corresponding tissue sections (cyan boundaries). Color bars are shown for combined, locally, and globally normalized decorrelation at the upper left, ranging from -4 to -1 ($\log_{10}$-scaled decorrelation per ms), and for IBS at the upper right, ranging from 0 to 8 dB.

predicted and measured ablation zones for the same trial and plane illustrated in Fig. 2 (trial B).

Table II summarizes statistical results for unsupervised prediction of ablation zones by weighted K-means clustering. Absolute and normalized RMS errors of predicted volumes ranged from 1.27 ml (23.5%) for globally normalized echo decorrelation to 2.09 ml (38.9%) for IBS. Correlation coefficients between predicted and measured ablation zone volumes across all trials ($N = 14$) were positive but not statistically significant for all predictors and were substantially greater for the echo decorrelation parameters (0.269–0.333) than for IBS (0.110). Mean Dice coefficients between predicted and measured ablation zones were similar for the three echo decorrelation parameters (0.662–0.676) but substantially higher than that for IBS (0.597), a statistically significant difference ($p < 10^{-3}$). The only statistically significant difference between Dice coefficients for the echo decorrelation predictors was a marginally higher coefficient for combined decorrelation, compared to globally normalized decorrelation ($p = 0.0165$).

IV. DISCUSSION

Echo decorrelation imaging in 2D has previously been verified for thermal ablation monitoring and control.[21,25–31,35,41] The present study shows the potential of 3D

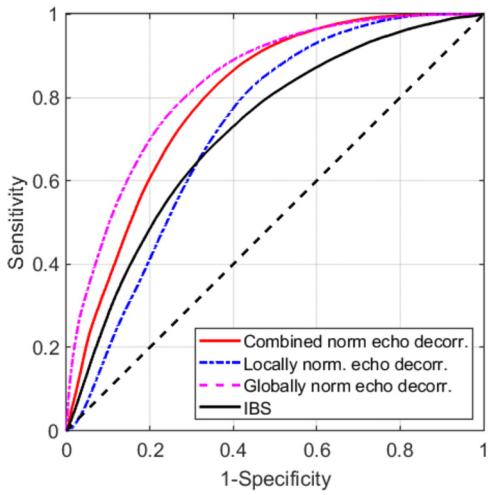

FIG. 3. (Color online) ROC curves illustrating performance in prediction of tissue ablation using combined echo decorrelation, locally and globally normalized echo decorrelation, and IBS.

echo decorrelation imaging for monitoring clinical RFA of liver, as well as similar bulk ablation approaches such as microwave ablation. All investigated image parameters predicted local ablation significantly better than chance, as assessed by ROC curve analysis ($p < 10^{-16}$). AUC values observed here fell within ranges previously observed for 2D imaging of comparable *ex vivo* RFA and bulk ultrasound ablation. For locally normalized, globally normalized, and combined 3D echo decorrelation, AUC covered the range 0.726–0.837, all within the range 0.722–0.919 attained in previous studies of 2D echo decorrelation imaging.[21,27,41] Similarly, AUC for IBS was 0.719, within the range 0.576–0.893 for previous studies of 2D echo decorrelation imaging.[21,41]

Notably, AUC for ablation prediction using echo decorrelation was relatively high in this study, even though echo decorrelation images were acquired only once every 11 s and scan line density (55×54 scan lines, compared to 2D B-mode imaging with over 100 scan lines in a single plane). Comparable AUC values have previously been reported by studies of 2D echo decorrelation imaging of *ex vivo* RFA employing higher frame rates, e.g., AUC of 0.855 for 1.2 echo decorrelation frames per second[21] and 0.919 for 9 frames per second.[41] Similarly, AUC of 0.719 found here for IBS was comparable to values of 0.592 and 0.893 in the same two studies.[21,41] In these previous two studies of 2D imaging, echo decorrelation and IBS parameters had been estimated using a temporal running average, thus improving reliability of parameter estimates. Here, although no temporal averaging was performed, relatively high AUC values for 3D echo decorrelation and IBS imaging suggest that computations within a 3D Gaussian correlation window accomplished substantial spatial averaging, as previously observed in simulations.[33]

Multiple previous studies of 2D echo decorrelation imaging for thermal ablation monitoring have employed the combined echo decorrelation parameter defined here,[25–28,41] while other studies have employed an equivalent of the locally normalized decorrelation parameter defined here.[29,31,34,42] Results of the present study suggest that alternative normalizations may also be appropriate for monitoring of RFA. Globally normalized echo decorrelation, defined by Eq. (6) to incorporate normalization by spatially averaged echo autocorrelation, showed the best predictive ability among the four predictors considered (AUC = 0.837, $p < 10^{-12}$ vs combined echo decorrelation). Globally normalized echo decorrelation also showed the best qualitative correspondence with local tissue ablation, as seen in Fig. 2 where this parameter corresponded more closely with observed ablation zones than the other three predictors. However, the three echo decorrelation normalizations investigated here resulted in similar monitoring performance in some respects. Optimal thresholds for local ablation prediction, corresponding to the point on each ROC curve nearest the top left corner, were close for all three decorrelation parameters, as seen in Table I.

Correlation coefficients between instantaneous parameter values and local tissue temperature were higher for globally normalized echo decorrelation (0.519) than for other predictors (0.435–0.502). Relations between each predictor and local temperature were statistically significant but weak, as seen in Fig. 5. This suggests that 3D echo decorrelation and IBS are not direct predictors of local temperature. This result is consistent with previous studies finding that tissue temperature is significantly but weakly correlated with echo decorrelation and IBS.[21,41]

Similarly, comparisons between measured ablation zone volumes and those predicted by weighted K-means segmentation were similar for all three echo decorrelation normalizations (normalized RMS errors 23.5%–27.3%), all of which showed better prediction of ablation volumes compared to IBS (normalized RMS error 38.7%). Dice coefficients between predicted

TABLE I. Statistical results for ROC curve analysis for combined echo decorrelation (Δ_C), locally normalized echo decorrelation (Δ_L), globally normalized echo decorrelation (Δ_G), and IBS. Shown are AUC, threshold for optimal prediction of local ablation, and p values for DeLong's test comparing AUC between predictors, with statistically significant values highlighted by bold text.

Prediction parameter	AUC	Optimal threshold	p value vs. AUC = 0.5	p value vs. Δ_L	p value vs. Δ_G	p value vs. IBS
Δ_C	0.801	−3.71 [$\log_{10}\Delta$/ms]	**$<10^{-16}$**	**$<10^{-16}$**	**$2.42 \cdot 10^{-11}$**	**$3.02 \cdot 10^{-6}$**
Δ_L	0.726	−3.66 [$\log_{10}\Delta$/ms]	**$<10^{-16}$**	–	**$<10^{-16}$**	0.704
Δ_G	0.837	−3.57 [$\log_{10}\Delta$/ms]	**$<10^{-16}$**	–	–	**$4.04 \cdot 10^{-13}$**
IBS	0.719	2.64 dB	**$<10^{-16}$**	–	–	–

https://doi.org/10.1121/10.0011641

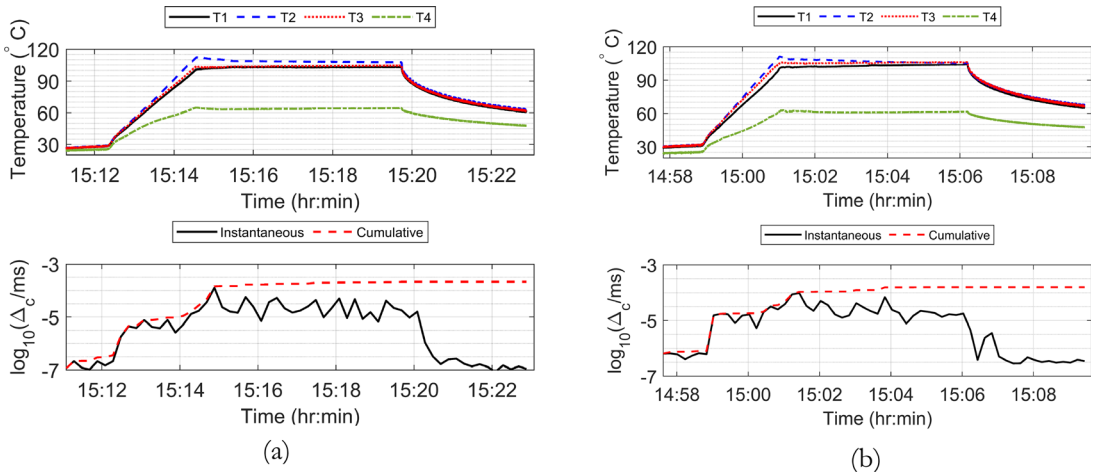

FIG. 4. (Color online) Time-dependent temperatures read from four thermocouples integrated into the RFA probe, with corresponding $\log_{10}$-scaled combined normalized instantaneous and cumulative echo decorrelation per ms, each spatially averaged over the computational ROI employed. Results for two representative ablation trials are shown as panels (a) and (b).

and measured ablation zones had means between 0.662 and 0.676 for the echo decorrelation predictors, indicating substantial agreement,[40] and mean ± standard deviation 0.597 ± 0.125 for IBS, indicating moderate to substantial agreement.[40] More sophisticated prediction approaches, e.g., employing machine-learning techniques,[43] could result in more accurate estimation of total ablated volume and ablation zone margins from measured echo decorrelation or IBS data.

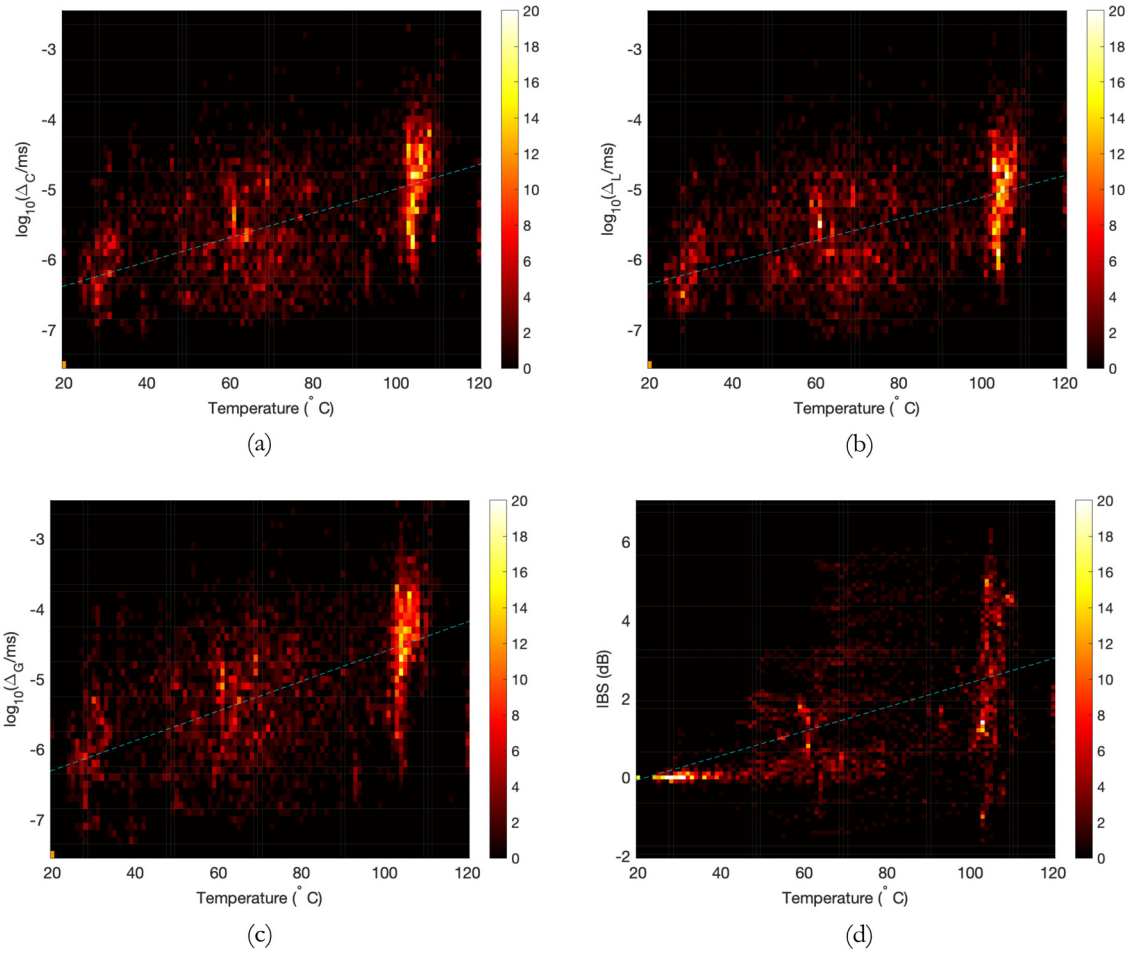

FIG. 5. (Color online) Histogram plots of (a) combined, (b) locally normalized, (c) globally normalized echo decorrelation, and (d) IBS versus temperature at four thermometer sensors for all 14 trials. The color bar shown, identical for all plots, indicates the number of data points (out of 3360 total points) falling within each histogram bin. Dashed lines show the best fit between predictors and temperature, computed by linear regression.

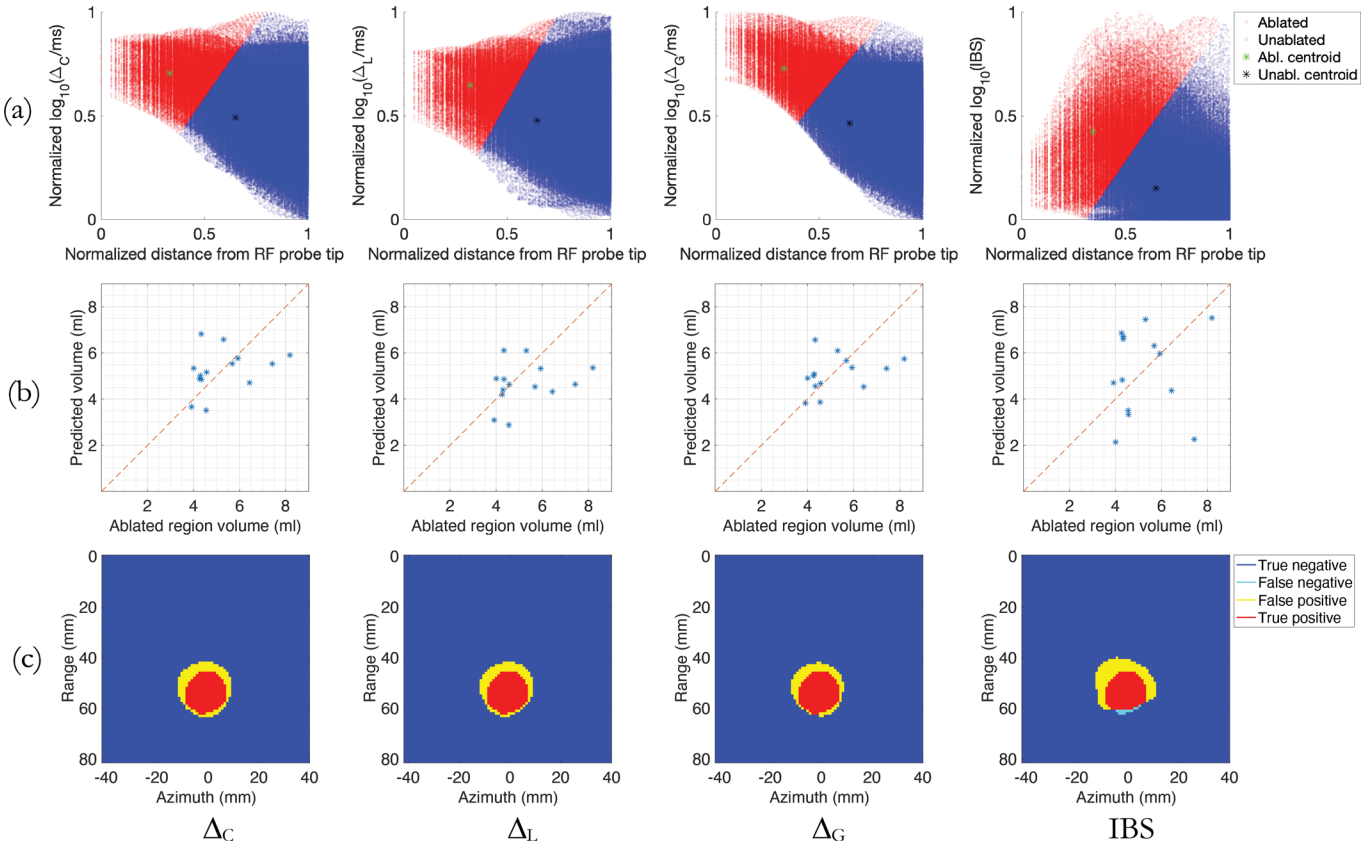

FIG. 6. (Color online) Prediction of ablation zone volumes and margins using weighted K-means clustering (weight $w = 0.8$). The four columns show results for each of the four predictors considered, labeled as in Fig. 2. (a) Final clusters comprising predicted ablated and unablated regions predicted by imaging parameters, with centroids for each. (b) Scatter plots of predicted vs measured ablation zone volume for all 14 trials. (c) Cross-sections of predicted and measured ablation zones for a representative trial [Fig. 2(b)].

Sources of uncertainty in these measurements included imprecision of the method employed for tissue sectioning. Since ablated tissue was sectioned with a slice thickness of 3–4 mm, the resulting reconstructed 3D ablation zone was coarsely sampled in the elevation direction. This resulted in uncertainty in estimating the position of the RFA needle tip, potentially causing registration error along the elevation direction. Some misalignments likely resulted between decorrelation and IBS maps and corresponding tissue sections. In addition, since the ablation zone volume is measured after freezing of tissue, some error may be caused by expansion tissue surrounding the ablation zone, changing the ablation zone shape to some extent. Use of finer sectioning or 3D interpolation of the mapped ablation zones could result in better correspondence between predicted and measured ablation, and thus higher AUC values for all predictors. In addition, assessment of the ablation zone from ablated tissue histology is limited because the tissue may contract as it loses water during thermal ablation, as has been observed by CT imaging during *ex vivo* microwave ablation.[44]

Another source of uncertainty during ultrasound imaging of *in vivo* and clinical thermal ablation is tissue motion due to respiration. To mitigate motion-induced decorrelation, echo volumes can potentially be acquired at specific time points during the breathing cycle, for example at the end of the exhale phase, either manually or by automatic gating. It has also been shown in previous experimental and

TABLE II. Statistical results for prediction of ablation zone using weighted K-means clustering. Shown for each predictor are the normalized RMS error, correlation coefficient for predicted vs measured ablation zone volumes across all trials, as well as Dice coefficients (mean ± standard deviation) for predicted vs measured ablation zones.

Prediction parameter	RMS volume error (ml)	Normalized RMS volume error (%)	Correlation coefficient r	Dice coefficient (mean ± standard deviation)
Δ_C	1.31	24.3%	0.323	0.676 ± 0.0882
Δ_L	1.41	27.3%	0.269	0.670 ± 0.0852
Δ_G	1.27	23.5%	0.333	0.662 ± 0.0998
IBS	2.09	38.9%	0.110	0.597 ± 0.125

simulation-based studies that motion effects can be compensated by separate measurements of motion-induced decorrelation.[34,45] Notably, integrated backscatter may be less sensitive to motion due to its dependence on echo amplitude rather than echo waveforms, potentially making it more suitable for imaging during respiration. Although the predictive capability of IBS (AUC = 0.719) was inferior to globally normalized echo decorrelation imaging (AUC = 0.837) and previous studies have generally shown better ablation prediction from echo decorrelation than IBS,[21,27,41] this potential insensitivity to motion may be useful in clinical practice.

During clinical RFA treatment, thermal coagulative necrosis is typically targeted to a region enclosing an entire tumor plus a tissue margin. To avoid overtreatment, potentially damaging major liver structures such as the hepatic artery, or undertreatment, potentially resulting in cancer recurrence, monitoring ablation progress in 3D is desirable. Implementation of echo decorrelation imaging as a built-in feature on clinical ultrasound scanners, with computational cost comparable to color and power Doppler imaging, would enable true real-time echo decorrelation imaging, e.g., with volumetric frame rates >10 Hz. The resulting improvements in temporal resolution of echo decorrelation imaging may further increase its ability to predict local ablation and overall ablation progress. Although echo decorrelation imaging only provides real-time feedback during the ablation process, additional ultrasound imaging methods, such as elastography[14,15] or contrast-enhanced imaging,[12,46] could also be employed using the same scanning system to assess and quantify the ablation zone after treatment is complete.

To reduce dependence of treatment outcomes on operator skill and to increase the precision of these procedures, automatic control of thermal ablation procedures has been proposed.[27,35,42,45] In one potential approach to control RFA using echo decorrelation imaging, a predictor value is measured at each voxel inside an ROI and either its minimum or average value is used as the treatment end point.[27] Optimal thresholds from ROC curve analysis in this study can be potentially used as endpoints for control of the tumor ablation. To confirm local ablation of malignant tissue and avoid recurrence, it may be appropriate to choose thresholds corresponding to higher specificity of local ablation prediction. For example, in a study of *ex vivo* bovine liver ablation by focused ultrasound, treatments were stopped when the minimum echo decorrelation inside a control ROI reached a specific threshold chosen for 90% specificity and 83% sensitivity of local ablation prediction based on ROC curve analysis.[35]

V. CONCLUSION

3D monitoring of *ex vivo* RFA of bovine liver was investigated using 3D echo decorrelation imaging with three different normalization methods, along with 3D integrated backscatter. All investigated image parameters showed statistically significant capability for prediction of local ablation, with the best performance attained by globally normalized echo decorrelation. When combined with a weighted K-means clustering algorithm to segment ablation zones, all definitions of echo decorrelation resulted in substantial agreement with measured ablation zones, as quantified by the Dice coefficient. All four investigated image parameters were significantly but weakly correlated with local tissue temperature. These results indicate the promise of 3D echo decorrelation and IBS imaging for real-time monitoring and control of radiofrequency and microwave tumor ablation procedures.

ACKNOWLEDGMENT

This work was supported by the National Institutes of Health (NIH) Grant No. R01 CA158439.

[1]S. McDermott and D. A. Gervais, "Radiofrequency ablation of liver tumors," Seminars Intervent. Radiol. **30**(1), 49–55 (2013).
[2]P. Tinguely, L. Frehner, A. Lachenmayer, V. Banz, S. Weber, D. Candinas, and M. H. Maurer, "Stereotactic image-guided microwave ablation for malignant liver tumors—A multivariable accuracy and efficacy analysis," Front. Oncol. **10**, 842 (2020).
[3]S. Y. Chiou, J. B. Liu, and L. Needleman, "Current status of sonographically guided radiofrequency ablation techniques," J. Ultrasound Med. **26**(4), 487–499 (2007).
[4]G. N'Kontchou, A. Mahamoudi, M. Aout, N. Ganne-Carrié, V. Grando, E. Coderc, E. Vicaut, J. C. Trinchet, N. Sellier, M. Beaugrand, and O. Seror, "Radiofrequency ablation of hepatocellular carcinoma: Long-term results and prognostic factors in 235 Western patients with cirrhosis," Hepatology **50**(5), 1475–1483 (2009).
[5]D. H. Lee and J. M. Lee, "Recent advances in the image-guided tumor ablation of liver malignancies: Radiofrequency ablation with multiple electrodes, real-time multimodality fusion imaging, and new energy sources," Korean J. Radiol. **19**(4), 545–559 (2018).
[6]Y. S. Kim, H. Rhim, O. K. Cho, B. H. Koh, and Y. Kim, "Intrahepatic recurrence after percutaneous radiofrequency ablation of hepatocellular carcinoma: Analysis of the pattern and risk factors," Eur. J. Radiol. **59**(3), 432–441 (2006).
[7]Y. M. Lin, I. Paolucci, K. K. Brock, and B. C. Odisio, "Image-guided ablation for colorectal liver metastasis: Principles, current evidence, and the path forward," Cancers **13**(16), 3926 (2021).
[8]A. Napoli, M. Anzidei, F. Ciolina, E. Marotta, B. Cavallo Marincola, G. Brachetti, L. Di Mare, G. Cartocci, F. Boni, V. Noce, L. Bertaccini, and C. Catalano, "MR-guided high-intensity focused ultrasound: Current status of an emerging technology," Cardiovasc. Intervent. Radiol. **36**(5), 1190–1203 (2013).
[9]C. H. Cha, F. T. Lee, Jr., J. M. Gurney, B. K. Markhardt, T. F. Warner, F. Kelcz, and D. M. Mahvi, "CT versus sonography for monitoring radiofrequency ablation in a porcine liver," Am. J. Roentgenol. **175**(3), 705–711 (2000).
[10]L. H. Lee, J. I. Hwang, Y. C. Cheng, C. Y. Wu, S. W. Lee, S.-S. Yang, H. Z. Yeh, C.-S. Chang, and T. Y. Lee, "Comparable outcomes of ultrasound versus computed tomography in the guidance of radiofrequency ablation for hepatocellular carcinoma," PLoS One **12**(1), e0169655 (2017).
[11]H. Tanaka, "Current role of ultrasound in the diagnosis of hepatocellular carcinoma," J. Med. Ultrasonics **47**(2), 239–255 (2020).
[12]E. J. Kim, Y. S. Kim, S. K. Shin, O. S. Kwon, D. J. Choi, and J. H. Kim, "Contrast-enhanced ultrasound-guided radiofrequency ablation in inconspicuous hepatocellular carcinoma on B-mode ultrasound," Turk. J. Gastroenterol. **28**(6), 446–452 (2017).
[13]S. Zhang, M. Wan, H. Zhong, C. Xu, Z. Liao, H. Liu, and S. Wang, "Dynamic changes of integrated backscatter, attenuation coefficient and bubble activities during high-intensity focused ultrasound (HIFU) treatment," Ultrasound Med. Biol **35**(11), 1828–1844 (2009).
[14]O. Kolokythas, T. Gauthier, A. T. Fernandez, H. Xie, B. A. Timm, C. Cuevas, M. K. Dighe, L. M. Mitsumori, M. F. Bruce, D. A. Herzka, G. K. Goswami, R. T. Andrews, K. M. Oas, T. J. Dubinsky, and B. H. Warren,

"Ultrasound-based elastography: A novel approach to assess radio frequency ablation of liver masses performed with expandable ablation probes: A feasibility study," J. Ultrasound Med. **27**(6), 935–946 (2008).
[15]W. Yang, T. Varghese, T. T. Ziemlewicz, M. Alexander, M. Lubner, J. L. Hinshaw, S. Wells, and F. T. Lee, "Post-procedure evaluation of microwave ablations of hepatocellular carcinoma using electrode displacement elastography," Ultrasound Med. Biol. **42**(12), 2893–2902 (2016).
[16]R. Seip and E. S. Ebbini, "Noninvasive estimation of tissue temperature response to heating fields using diagnostic ultrasound," IEEE Trans. Biomed. Eng. **42**(8), 828–839 (1995).
[17]T. Varghese, J. A. Zagzebski, Q. Chen, U. Techavipoo, G. Frank, C. Johnson, A. Wright, and F. T. Lee, Jr., "Ultrasound monitoring of temperature change during radiofrequency ablation: Preliminary *in-vivo* results," Ultrasound Med. Biol. **28**(3), 321–329 (2002).
[18]J. Civale, I. Rivens, G. ter Haar, H. Morris, C. Coussios, P. Friend, and J. Bamber, "Calibration of ultrasound backscatter temperature imaging for high-intensity focused ultrasound treatment planning," Ultrasound Med. Biol. **39**(9), 1596–1612 (2013).
[19]C. H. Seo, Y. Shi, S.-W. Huang, K. Kim, and M. O'Donnell, "Thermal strain imaging: A review," Interface Focus **1**, 649–664 (2011).
[20]P. Baki, S. J. Sanabria, G. Kosa, G. Szekely, and O. Goksel, "Thermal expansion imaging for monitoring lesion depth using M-mode ultrasound during cardiac RF ablation: In vitro study," Int. J. Comput. Assist. Radiol. Surg. **10**(6), 681–693 (2015).
[21]T. D. Mast, D. P. Pucke, S. E. Subramanian, W. J. Bowlus, S. M. Rudich, and J. F. Buell, "Ultrasound monitoring of in vitro radio frequency ablation by echo decorrelation imaging," J. Ultrasound Med. **27**(12), 1685–1697 (2008).
[22]I. Cespedes, J. Ophir, and S. K. Alam, "The combined effect of signal decorrelation and random noise on the variance of time delay estimation," IEEE Trans. Ultrason. Ferroelectr. Freq. Control **44**(1), 220–225 (1997).
[23]J. C. Bamber and C. R. Hill, "Ultrasonic attenuation and propagation speed in mammalian tissues as a function of temperature," Ultrasound Med. Biol. **5**(2), 149–157 (1979).
[24]V. Suomi, Y. Han, E. Konofagou, and R. O. Cleveland, "The effect of temperature dependent tissue parameters on acoustic radiation force induced displacements," Phys. Med. Biol. **61**(20), 7427–7447 (2016).
[25]S. Subramanian, S. M. Rudich, A. Alqadah, C. P. Karunakaran, M. B. Rao, and T. D. Mast, "*In vivo* thermal ablation monitoring using ultrasound echo decorrelation imaging," Ultrasound Med. Biol. **40**(1), 102–114 (2014).
[26]Z. Zhou, Y. Wang, S. Song, W. Wu, S. Wu, and P.-H. Tsui, "Monitoring microwave ablation using ultrasound echo decorrelation imaging: An *ex vivo* study," Sensors **19**(4), 977 (2019).
[27]M. A. Abbass, A. J. Garbo, N. Mahalingam, J. K. Killin, and T. D. Mast, "Optimized echo decorrelation imaging feedback for bulk ultrasound ablation control," IEEE Trans. Ultrason. Ferroelectr. Freq. Control **65**(10), 1743–1755 (2018).
[28]M. S. R. Gudur, R. Kumon, Y. Zhou, and C. X. Deng, "High-frequency rapid B-mode ultrasound imaging for real-time monitoring of lesion formation and gas body activity during high-intensity focused ultrasound ablation," IEEE Trans. Ultrason. Ferroelectr. Freq. Control **59**(8), 1687–1699 (2012).
[29]R. Matsuzawa, T. Shishitani, S. Yoshizawa, and S. I. Umemura, "Monitoring of lesion induced by high-intensity focused ultrasound using correlation method based on block matching," Jpn. J. Appl. Phys. **51**, 07GF26 (2012).
[30]R. Kumon, M. S. R. Gudur, Y. Zhou, and C. X. Deng, "High-frequency ultrasound M-mode imaging for identifying lesion and bubble activity during high-intensity focused ultrasound ablation," Ultrasound Med. Biol. **38**(4), 626–641 (2012).
[31]S. Sasaki, R. Takagi, K. Matsuura, S. Yoshizawa, and S. I. Umemura, "Monitoring of high-intensity focused ultrasound lesion formation using decorrelation between high-speed ultrasonic images by parallel beamforming," Jpn. J. Appl. Phys. **53**(7), 07KF10 (2014).
[32]C. Papadacci, E. A. Bunting, and E. E. Konofagou, "3D quasi-static ultrasound elastography with plane wave *in vivo*," IEEE Trans. Med. Imag. **36**(2), 357–365 (2017).
[33]M. T. Cox, M. A. Abbass, and T. D. Mast, "Numerical analysis of three-dimensional echo decorrelation imaging," J. Acoust. Soc. Am. **147**(6), EL478–EL483 (2020).
[34]F. M. Hooi, A. Nagle, S. Subramanian, and T. D. Mast, "Analysis of tissue changes, measurement system effects, and motion artifacts in echo decorrelation imaging," J. Acoust. Soc. Am. **137**(2), 585–597 (2015).
[35]M. A. Abbass, J. K. Killin, N. Mahalingam, F. M. Hooi, P. G. Barthe, and T. D. Mast, "Real-time spatiotemporal control of high-intensity focused ultrasound thermal ablation using echo decorrelation imaging in *ex vivo* bovine liver," Ultrasound Med. Biol. **44**(1), 199–213 (2018).
[36]D. J. H. Wojtek and J. Krzanowski, *ROC Curves for Continuous Data* (Chapman & Hall/CRC, Boca Raton, FL, 2009), pp. 17–21.
[37]J. A. Hanley and B. J. McNeil, "The meaning and use of the area under a receiver operating characteristic (ROC) curve," Radiology **143**(1), 29–36 (1982).
[38]E. R. DeLong, D. M. DeLong, and D. L. Clarke-Pearson, "Comparing the areas under two or more correlated receiver operating characteristic curves: A nonparametric approach," Biometrics **44**(3), 837–845 (1988).
[39]G. N. Abras and V. L. Ballarin, "A weighted K-means algorithm applied to brain tissue classification," J. Comp. Sci. Technol. **5**(3), 121–126 (2005).
[40]J. R. Landis and G. G. Koch, "The measurement of observer agreement for categorical data," Biometrics **33**, 159–174 (1977).
[41]S. Subramanian, D. T. Schmidt, M. B. Rao, and T. D. Mast, "Dependence of ultrasound echo decorrelation on local tissue temperature during *ex vivo* radiofrequency ablation," Phys. Med. Biol. **61**(6), 2356–2371 (2016).
[42]R. Takagi, H. Jimbo, R. Iwasaki, K. Tomiyasu, S. Yoshizawa, and S. I. Umemura, "Feasibility of real-time treatment feedback using novel filter for eliminating therapeutic ultrasound noise with high-speed ultrasonic imaging in ultrasound-guided high-intensity focused ultrasound treatment," Jpn. J. Appl. Phys. **55**(7), 07KC10 (2016).
[43]S. Zhang, S. Wu, S. Shang, X. Qin, X. Jia, D. Li, Z. Cui, T. Xu, G. Niu, A. Bouakaz, and M. Wan, "Detection and monitoring of thermal lesions induced by microwave ablation using ultrasound imaging and convolutional neural networks," IEEE J. Biomed. Health Inform. **24**(4), 965–973 (2020).
[44]D. Liu and C. L. Brace, "CT imaging during microwave ablation: Of spatial and temporal tissue contraction," Med. Phys. **41**(11), 113303 (2014).
[45]M. A. Abbass, S. A. Ahmad, N. Mahalingam, K. S. Krothapalli, J. A. Masterson, M. B. Rao, P. G. Barthe, and T. D. Mast, "*In vivo* ultrasound thermal ablation control using echo decorrelation imaging in rabbit liver and VX2 tumor," PLoS One **14**, e0226001 (2019).
[46]C. P. Nolsøe, A. B. Nolsøe, J. Klubien, H. C. Pommergaard, J. Rosenberg, M. F. Meloni, and T. Lorentzen, "Use of ultrasound contrast agents in relation to percutaneous interventional procedures: A systematic review and pictorial essay," J. Ultrasound Med. **37**(6), 1305–1324 (2018).